Korean J. Chem. Eng., **31**(8), 1339-1348 (2014)
DOI: 10.1007/s11814-014-0090-7

pISSN: 0256-1115
eISSN: 1975-7220

Scale up criteria for dual stirred gas-liquid unbaffled tank with concave blade impeller

Thiyam Tamphasana Devi and Bimlesh Kumar†

Department of Civil Engineering, Indian Institute of Technology Guwahati, India
(*Received 21 December 2013 • accepted 25 March 2014*)

Abstract−Experimental investigation has been done in unbaffled gas-liquid stirred tanks using dual concave blade impeller to analyze the mass transfer, power consumption and gas holdup. Optimal impeller clearance has been suggested for lower and upper impeller based on maximum mass transfer rate. Numerical modeling has been done to analyze the flow pattern for different combinations of impeller clearance. The lower impeller positioned at 0.3 of tank diameter and clearance between lower and upper impeller at 0.4 of tank diameter gave the maximum mass transfer coefficient. Scale-up criteria for mass transfer rate, power and gas holdup have been developed for optimal geometrical similar systems of unbaffled stirred tanks with dual concave impeller.

Keywords: Clearance, Gas-liquid, Gas Holdup, Mass Transfer, Power, Stirred Tanks, Unbaffled

INTRODUCTION

Gas-liquid stirred reactors with multiple impellers are used in several industrial applications like fermentations, waste water treatment, hydrogenation, dissolution, etc. Compared with single impeller, the dual combination is more advantageous, with efficient gas distribution, higher gas phase residence time and lower power consumption per impeller [1]. Especially for uniform suspension of solids, the dual-impeller system is more energy-effective than the single impeller and needs lower rotational speed [2], which is very important in systems sensitive to shearing.

When more than one impeller is used, the flow complexity is greatly increased, especially when there is an interaction between flow generated by two impellers. The extent of interaction depends on relative distances between the two impellers (and clearance from the vessel bottom). Hudcova et al. [3] studied the influence of these flow patterns on the gross flow characteristics, such as power consumption and flow regime transition in a gas-liquid stirred vessel. The flows generated in stirred tanks with liquid depth equal to tank diameter provided with dual impeller agitation systems of impeller diameter equal to one third of tank diameter were studied by Rutherford et al. [4]. They identified three stable flow patterns: parallel, merging and diverging. Mahmoudi [5] determined that the merging flow pattern led to a mixing time lower by around 20% compared to the two others' patterns. This makes the merging flow pattern more attractive for mixing operations. Literature [6-11] is replete with the simulation and scale up criteria for stirred tank with dual Rushton impeller in baffled condition, but it is very less based on concave blade impeller. The concave blade impeller is a radial flow impeller like the Rushton turbine but with six curved blades on a disk rotating with the open concave portion at the lead, which performs better than conventional Rushton turbine [12-15]. The use of unbaffled stirred tanks may be desirable, for example, in crystallization operations where the presence of baffles may promote particle attrition [16], in precipitation processes where baffles could suffer encrustation problems [17], in biological operations where cell damage may be intensified with the presence of baffles [18], and in food and pharmaceutical industries where tank cleanliness is of primary importance [19]. Unbaffled stirred tanks give higher value of the mass transfer coefficient at the same power consumption than baffled tanks [20,21].

Thus, our aim was to evaluate the influence of the impeller clearance on mass transfer rate and to find the optimal impeller clearance in dual stirred unbaffled tank with concave blade impeller. The focus of this paper is to develop the scale-up criteria in geometrically similar stirred tank based on optimal impeller clearance. Computational fluid dynamics approach was applied to the optimal impeller clearance for observing the flow patterns and other relevant parameters.

EXPERIMENTATION

We tested two sizes of circular unbaffled tank of diameter (D) 200 mm and 150 mm under laboratory conditions (Fig. 1). Concave blade impellers with 0.3D were used in the experiments. The curvature angle of the impeller was 140^0. The blade height (b), the blade length (l) and the disc thickness were set as d/5, d/4 and 0.035d, respectively. The central disc diameter was 0.5d.

The liquid depth (H) in the stirred tank was maintained equal to the tank diameter in all experiments. The working fluid was water with density, ρ_w, of 1,000 kg/m^3. Rewatkar et al. [22] observed that a ring sparger of diameter equal to 0.8d gives the maximum gas holdup In the case of the ring sparger, a smaller number of holes and holes of a smaller size give a larger gas holdup [22]. A ring sparger of 0.8d with 6 holes of 2 mm diameter was used to supply air. The air supply from the compressor to the ring sparger was controlled by a valve. A rotameter was fixed before the valve to measure the volumetric flow rate (1 L/min and 5 L/min). The location of the sparger was fixed in each experiment at 0.09D from the bottom of the tank.

†To whom correspondence should be addressed.
E-mail: bimk@iitg.ernet.in

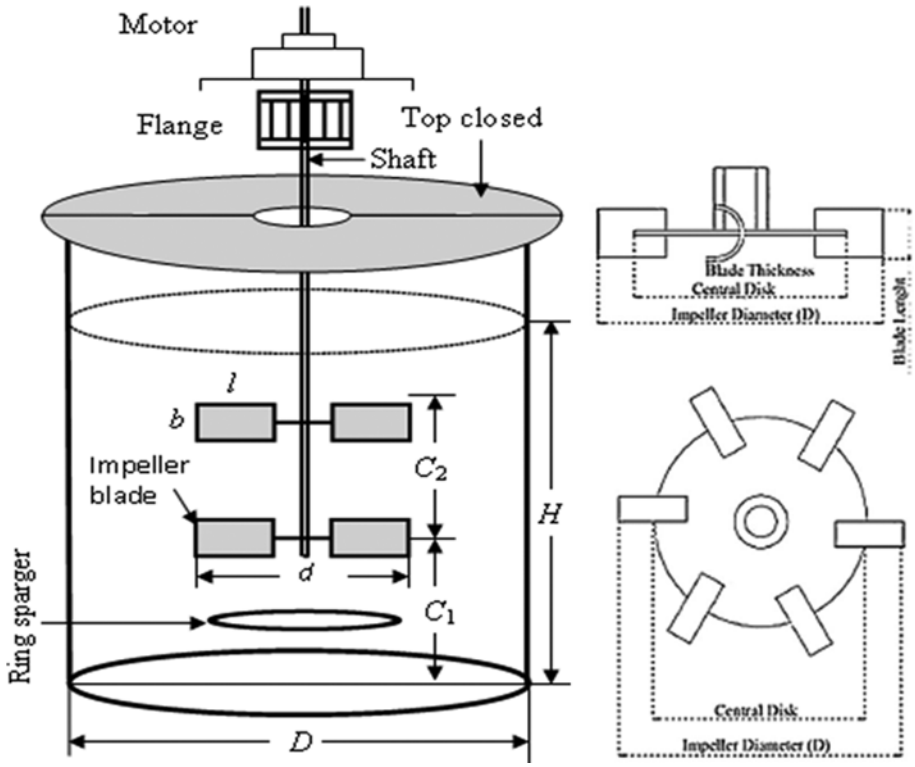

Fig. 1. Schematic diagram of an unbaffled sparged stirred tank.

1. Mass Transfer Coefficient

The standard dynamic method was used to measure volumetric mass transfer rate. For implementing the standard dynamic method, the liquid phase was deoxygenated by flushing with nitrogen. Then, after replacing nitrogen by air, the variation in dissolved oxygen concentrations with time was measured until reaching saturation. This technique is widely employed in the literature [23,24]. A Thermo Orion® DO meter, which was used to measure the concentration, has 0.1 mg/*l* accuracy in measurement. Assuming the liquid phase is well mixed and gas absorption is liquid phase controlled, the volumetric mass transfer coefficient at T°C (K_La_T) can be determined from following equation [25]:

$$K_La_T=[\ln(C_s-C_0)-\ln(C_s-C_t)]/t \quad (1)$$

where, ln represents natural logarithm and the concentrations C_s, C_0 and C_t are dissolved oxygen (DO) concentrations in parts per million (ppm), C_s=the saturation DO concentration at time tending to very large values, C_0 is at t=0 and C_t is at time t=t. Assuming the dynamics of the oxygen probe as a first-order differential equation, the time constant of the oxygen probe based on probe response to negative oxygen steps is found equal to 14 s, which is small compared to the mass transfer characteristics time. The overall mass transfer coefficient at a standard temperature of 20 °C is given by Patil et al. [26]:

$$K_La_{20}=K_La_T/\theta^{(T-20)} \quad (2)$$

where, θ is the temperature coefficient 1.02 for pure water.

2. Power Measurement

As Ascanio et al. [27] and Gogate et al. [1] reported, the most frequently used techniques for the evaluation of power consumption in stirred tanks and fermentors use watt meters, ammeters, colorimeters, dynamometers, torque meters and systems based on strain gauges. Each of these systems has its own advantages and disadvantages, and is chosen based on some factors such as investment, scale, precision, and range of measurement. As pointed out by King et al. [28], electrical measurements can be a suitable methodology, provided the power losses occurring in the motor and in the agitation system are known and subtracted from the total power draw. A Universal motor of 100 Kilowatts was used in the present work. Assuming steady state operation and for single phase motor, power output can be calculated as:

$$P_{output}=VI\cos\phi\,\eta \quad (3)$$

where, V=input voltage, I=input current, η=efficiency and $\cos\phi$= power factor (P_f).

Based on motor internal parameters, curves were generated to determine the efficiency and power factor for the measured speed. Thus the mechanical power was calculated.

Gas holdup was measured by visual method [26]. A graduated graph paper was pasted on the outside of the vessel. By noting the difference between level with and without aeration the holdup was found. The following equation was used.

$$\varepsilon_G=(H_G-H)/H_G \quad (4)$$

where H_G=Height of liquid after aeration (m), H=Height of clear liquid without aeration (m) and ε_G=gas holdup.

RESULTS AND DISCUSSION

In this section, the identification of impeller clearance distance

(C_1) and their spacing (C_2) based on experimentally observed K_La_{20} will be presented and discussed. Experiments have been done in two steps, with and without sparging condition, which is required for scaling up the results. By setting geometrical parameters as mentioned above, initial runs were performed without sparging condition and power consumption was measured. Power consumption without sparging (P_u) is required for scaling up the power results. When the sparger is placed below the impeller, it favors the gas to be entrained into the circulation loop present in the lower part of the tank. The gas then has a longer residence time in the vessel, which promotes mass transfer. However, the gap between sparger location and impeller clearance has an important effect on mass transfer. The gap should be sufficient to break up the bubbles and to disperse the gas throughout the vessel. Keeping this in view, the initial value C_1 was chosen as 0.25D. Once again, experiments were conducted with sparged condition and process variables (mass transfer rate, power consumption with sparging (P_g) and gas holdup) were measured.

1. Optimal C_1 and C_2 Based on K_La_{20}

By fixing d/D=0.3, the selection of C_1 and C_2 is achieved through univariant approach (fixing one variable while the other variable is changing). Experiments were performed by fixing C_1 at 0.25D while C_2 was changing from 0.2D to 0.6D at different impeller speed (N= 300 to 800 rpm). The variation of measured K_La_{20} on different C_2 values while C_1 was fixed as shown in Fig. 2.

It is observed that highest K_La_{20} was measured at C_2=0.4D. Note that the bottom clearance of the upper impeller is equal to 0.7D. Further experiments were done by fixing the upper impeller at 0.7D (S_2) and changing C_1 (0.25-0.45D). Fig. 3 depicts the variation of K_La_{20} at different C_1/D ratios, and the optimal point of C_1 is observed at 0.3D. So, the second optimal of C_1 and C_2 is 0.3D and 0.4D, respectively.

Same procedure was done by fixing C_1 at 0.3D, 0.35D, 0.4D and 0.45D, as shown in Fig. 4.

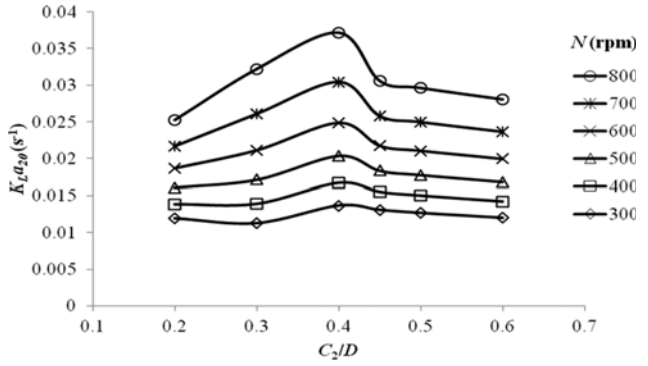

Fig. 2. Variation of K_La_{20} for different C_2/D at C_1=0.25D.

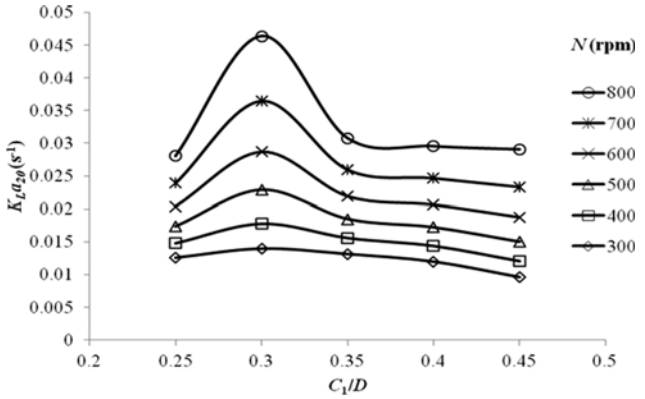

Fig. 3. Variation of K_La_{20} for different C_1/D at S_2=0.7D.

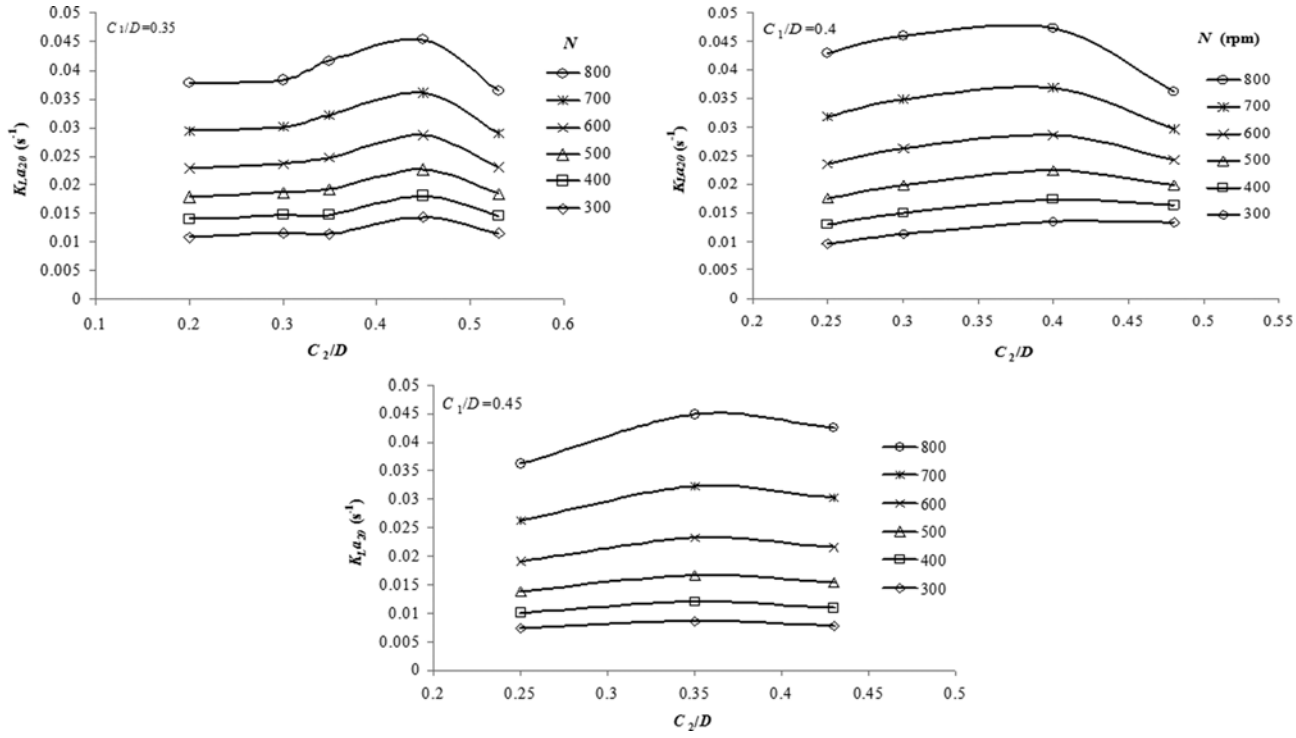

Fig. 4. Variation of K_La_{20} for different C_1/D.

Table 1. Optimal configurations of C_1 and C_2 based on K_La_{20}

C_1	C_2	K_La_{20} at 500 rpm	Remarks on optimal
0.25D	0.4D	0.0204	Local
0.3D	0.4D	0.0229	Highest K_La_{20} (global)
0.35D	0.45D	0.0227	Local
0.4D	0.4D	0.0223	Local
0.45D	0.35D	0.0167	Local

Table 1 enlists the values of K_La_{20} at constant speed on each C_1 and C_2. From Table 1, the global optimal C_1 and C_2 is at 0.3D and 0.4D, respectively, which gives highest K_La_{20} among the other configurations.

2. Numerical Modeling

Numerical modeling was done by computational fluid dynamics (CFD) to understand the flow patterns at different optimal configurations. Fig. 5 shows the generated grid of the double impeller stirred tank with sparging system (ring sparger) and its coarsened grid surface. CFD simulations were performed for 150 mm diameter tank at 500 rpm. The CFD code employed was FLUNET 6.3.26®.

Deglon and Meyer [29] studied various grid sizes (low coarse, coarse, medium fine and fine) on single impeller stirred tanks of having circular tank with 0.15 cm diameter and height and found that the medium fine grid showed good agreement with experimental results. They also concluded that the fine grid showed little improvement in the result. It is also a fact that the finer the grid, the higher the simulation cost. So, they concluded, in order to save computational cost, the medium fine grid can be used in prediction of flow fields; however, accurate predictions of turbulence required finer grids. Unstructured (tetrahedral) medium fine grids of around 1100k cells were generated, considering the finer grid consumes longer time to simulate. To account for the complex fluid flow (turbulence) near the impeller region, the finer grid was adopted in this particular region instead of making finer whole of the vessel so that accurate turbulence could also be captured with reasonable computing time. The governing equation involved in two-phase modeling is the Eulerian-Eulerian approach [30]. The Eulerian-Eulerian multiphase model is widely used in the modeling of gas-liquid phase stirred tanks [31-33]. The phases (continuous and disperse) are treated as interpenetrating media identified by their local volume fractions. The volume fractions sum to unity and are calculated by using continuity equation. The Reynolds averaged mass and momentum balance equations are solved for each of the phases and are given as follows:

Continuity equation:

$$\frac{\partial}{\partial t}(\alpha_i\rho_i)+\nabla\cdot(\alpha_i\rho_i\vec{U}_i)=0 \tag{5}$$

$$\alpha_l+\alpha_g=1 \tag{6}$$

where, ρ_i, α_i and $\vec{U}_i$ are density, volume fraction and mean velocity, respectively, of phase i (l or g).

Momentum equation:

$$\frac{\partial}{\partial t}(\alpha_i\rho_i\vec{U}_i)+\nabla\cdot(\alpha_i\rho_i\vec{U}_i\vec{U}_i)=-\alpha_i\nabla p+\nabla\cdot\bar{\bar{\tau}}_{effi}+\vec{R}_i+\vec{F}_i+\alpha_i\rho_i\vec{g} \tag{7}$$

where, p is the pressure shared by the two phases and $\vec{R}_i$ is the interphase momentum exchange terms. $\vec{g}$ is the gravitational forces. $\vec{F}_i$, represents the Coriolis and centrifugal forces applied in MRF (multiple reference frame) impeller model, which is used in this study as the impeller model.

$$\vec{F}_i=-2\alpha_i\rho_i\vec{N}\times\vec{U}_i-\alpha_i\rho_i\vec{N}\times(\vec{N}\times\vec{r}) \tag{8}$$

where, $\vec{N}$ is angular velocity (rad s^{-1}) and $\vec{r}$ is position vector (m).

The Reynolds stress tensor $\bar{\bar{\tau}}_{effi}$ is the laminar and turbulent stresses, and by Boussinesq hypothesis, it is given as:

$$\bar{\bar{\tau}}_{effi}=\alpha_i(\mu_{lam,i}+\mu_{t,i})(\nabla\vec{U}_i+\nabla\vec{U}_i^T)-\frac{2}{3}\alpha_i(\rho_i k_i+(\mu_{lam,i}+\mu_{t,i})\nabla\cdot\vec{U}_i)\bar{\bar{I}} \tag{9}$$

$\mu_{lam,i}$ and $\mu_{t,i}$ are laminar and turbulent viscosity for phase i. k_i is turbulent kinetic energy for phase i and $\bar{\bar{I}}$ is unit tensor. The standard k-ε turbulence model is adequate for many engineering appli-

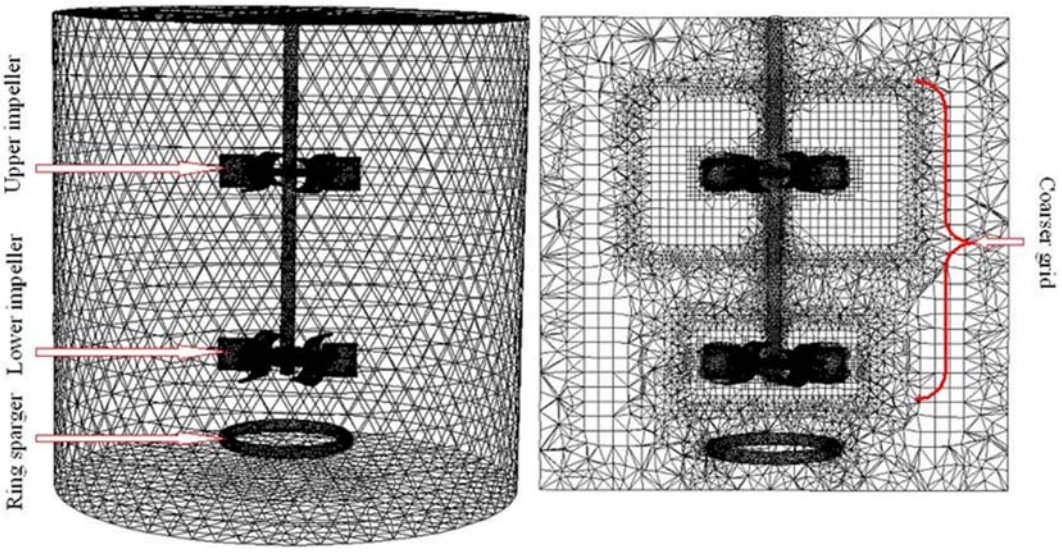

Fig. 5. Generated grid of the stirred tank.

cations [34] and is used in this study with dispersed k-ε multiphase turbulence model [35] to simulate the gas-liquid phase flow as gas (secondary phase) is dispersed in continuous liquid (primary phase). As the concentration of air phase is dilute in the water phase, the dispersed turbulence model is used here. Therefore, water phase turbulence is considered as the dominant turbulence potential. The governing equations of turbulent kinetic energy, k and turbulent dissipation rate, ε, are solved only for liquid phase as:

$$\frac{\partial}{\partial t}(\rho_l\alpha_l k_l)+\nabla\cdot(\rho_l\alpha_l\vec{U}_l k_l)=\nabla\cdot\left(\alpha_l\frac{\mu_{t,l}}{\sigma_k}\nabla k_l\right)+\alpha_l G_{kl}-\rho_l\alpha_l\varepsilon_l+\rho_l\alpha_l\Pi_{kl} \tag{10}$$

$$\frac{\partial}{\partial t}(\rho_l\alpha_l\varepsilon_l)+\nabla\cdot(\rho_l\alpha_l\vec{U}_l\varepsilon_l)=\nabla\cdot\left(\alpha_l\frac{\mu_{t,l}}{\sigma_\varepsilon}\nabla\varepsilon_l\right)+\alpha_l\frac{\varepsilon_l}{k_l}(C_{1\varepsilon}G_{kl}-C_{2\varepsilon}\rho_l\varepsilon_l)+\rho_l\alpha_l\Pi_{\varepsilon l} \tag{11}$$

Turbulent liquid viscosity is given as:

$$\mu_{t,l}=\rho_l C_\mu\frac{k_l^2}{\varepsilon_l} \tag{12}$$

G_{kl} is the rate of production of turbulent kinetic energy. Π_{kl} and $\Pi_{\varepsilon l}$ represent the influence of the dispersed phase on the continuous phase [36,37]. C_μ, $C_{1\varepsilon}$, $C_{2\varepsilon}$, $C_{3\varepsilon}$, σ_k and σ_ε are constants of the standard k-ε model. Their values are 0.09, 1.44, 1.92, 1.2, 1.0 and 1.3, respectively. Π_{kl} and $\Pi_{\varepsilon l}$ take into account the turbulence interaction between the water and air phases and modelled as:

$$\Pi_{kl}=\frac{C_D}{\alpha_l\rho_l}(C_{lg}-2k_l+\vec{U}_{lg}\cdot\vec{U}_{dr}) \tag{13}$$

where, C_{lg} is the covariance of the velocities of air and water; $\vec{U}_{lg}$ $(=\vec{U}_g-\vec{U}_l)$ is the relative velocity of air and water; and $\vec{U}_{dr}$ is the drift velocity.

$$C_{lg}=2k_l\left(\frac{b+\eta_{lg}}{1+\eta_{lg}}\right)$$
$$\vec{U}_{dr}=-\left(\frac{D_g}{\sigma_{lg}\alpha_g}\nabla\alpha_g-\frac{D_l}{\sigma_{lg}\alpha_l}\nabla\alpha_l\right) \tag{14}$$

Here, $b=(1+C_v)((\rho_l/\rho_g)+C_v)^{-1}$; $C_v=0.5$; D_g and D_l are diffusivities; and $\sigma_{lg}=0.75$ is a dispersion Prandtl number. Details of D_g, D_l and η_{lg} can be obtained from the work of Simonin and Violett [38].

According to Elgobashi and Rizk [36]:

$$\Pi_{\varepsilon l}=C_{3\varepsilon}\frac{\varepsilon_l}{k_l}\Pi_{kl} \tag{15}$$

where, $C_{3\varepsilon}=1.2$.

Drag force is the most important inter-phase force acting on the bubbles, resulting from the mean relative velocity between the two phases and an additional contribution, resulting from turbulent fluctuations in the volume fraction due to averaging of momentum equations. Considering only the drag force, $\vec{R}_i$ from Eq. (7) reduced only to drag force as:

$$\vec{R}_l=-\vec{R}_g=K(\vec{U}_g-\vec{U}_l) \tag{16}$$

K is the liquid-gas exchange co-efficient given as:

$$K=\frac{3}{4}\rho_l\alpha_l\alpha_g\frac{C_D}{d_b}\left|\vec{U}_g-\overleftarrow{U}_l\right| \tag{17}$$

d_b is the bubble diameter and C_D is the drag co-efficient defined as function of relative Reynolds number, Re_p. The standard formulation of Re_p does not account for the effect of turbulence on bubble movement. Hence, Re_p has been modified to include the effect of turbulence [39]:

$$Re_p=\frac{\rho_l\left|\vec{U}_g-\vec{U}_l\right|d_b}{\mu_l+C\mu_{t,l}} \tag{18}$$

C is the model parameter introduced to account for the effect of the turbulence in reducing slip velocity. This parameter is set to 0.3 [40]. Drag co-efficient is then calculated using standard correlation of Schiller and Naumann [41], which is written as:

$$C_D=\begin{cases}\dfrac{24(1+0.15Re_p^{0.687})}{Re_p}, & Re_p\le 1000\\ 0.44, & Re_p>1000\end{cases} \tag{19}$$

In the present work, the top surface of the sparger was modeled as velocity inlet and the appropriate gas velocity with gas volume fraction, equal to unity, was specified at the top surface of the sparger to simulate gas introduction in the vessel. Top surface is applied as degassing boundary condition through user-defined functions, which satisfies that the gas should escape from the computational domain and liquid (water) will remain inside the domain. Prediction of flow pattern for the different phases (liquid and gas) is an important parameter for understanding the flow structure of the turbulent flow when sparged condition is applied. Fig. 6(a)-(e) shows the flow pattern defined by mean velocity vectors for liquid (left) and gas phase (right) at different optimal configurations of C_1 and C_2. In all the cases, the liquid flow pattern is greatly affected by gas inflow of additional gas supply (Q_g=1 L/min) through ring sparger below the lower impeller. Maximum amount of intense liquid flow circulation is predicted near and around the impeller blade. The effect of gas inflow can be observed from this figure as the well known liquid flow circulation loop one below the blade and one above the blade are not created at all in this gas-liquid system. This is how the sparged system is different from a single phase system in terms of flow pattern. Instead of forming a liquid circulation loop above and below the impeller blade, these loops are seen created away from blades. The flow pattern in sparged condition of double impeller with concave blade impeller produces very uncommon and interesting flow pattern that is totally different from a single phase system. The only circulation loop that can be seen is on the upper part of the lower impeller. The upper impeller could make liquid circulation loop either above or below the blade. Enough space for fully circulation of liquid flow is not available above the blade by the upper impeller and hence could not make circulation loop above the blade. Due to the influence of lower impeller, a circulation loop could be created below the blade by the upper impeller. Also, by the lower impeller a circulation loop is not created below the blade due to the strong influence of gas inflow from sparger. The influence of gas inflow is more when impeller clearance depth (C_1) is lower. Smooth axial liquid flow circulation between the impeller is predicted when C_1 is not greater than 0.3D, but when C_1 is greater than 0.3D, the liquid flow

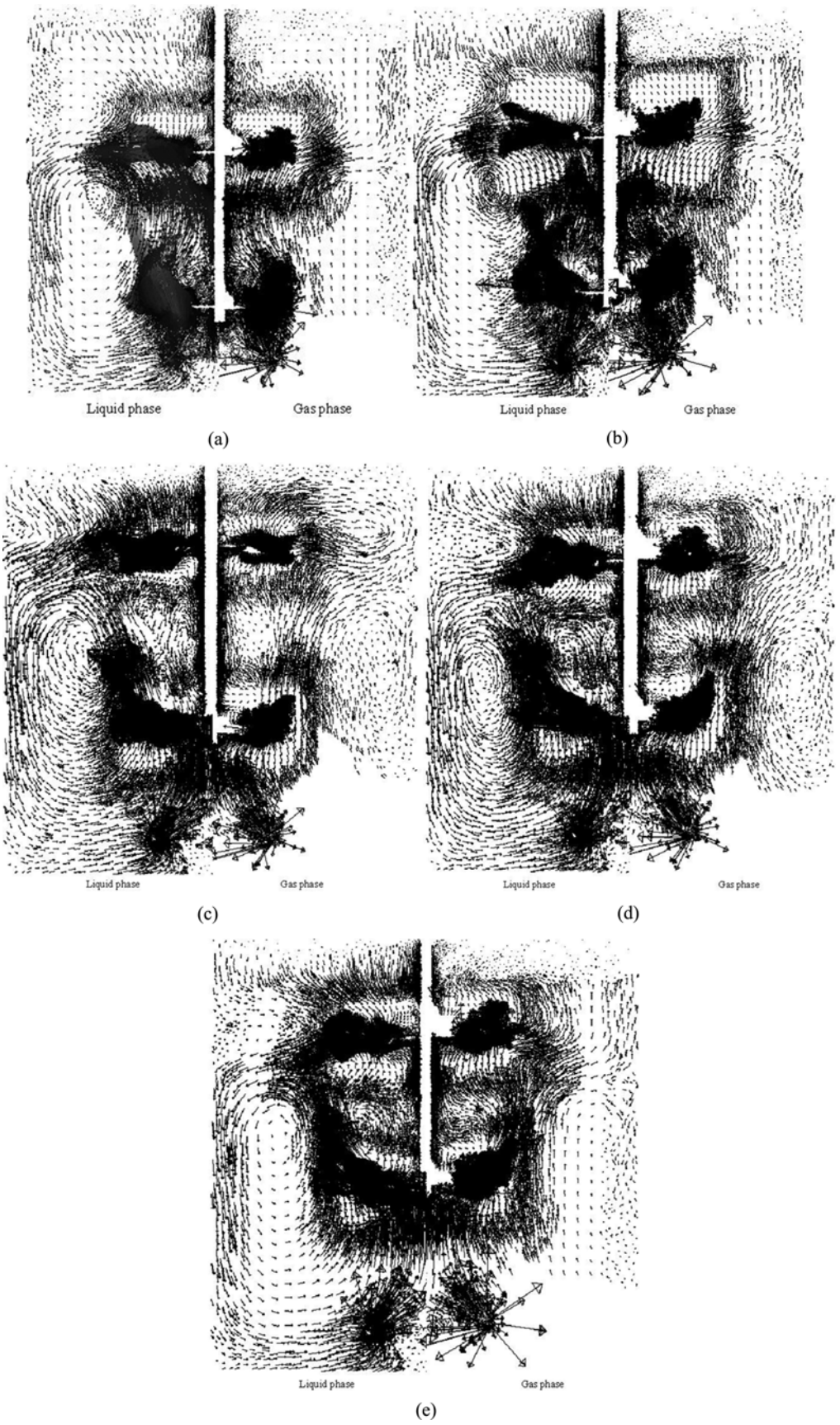

Fig. 6. Comparison of the velocity vectors of liquid phase and gas phase for (a)-(e) optimal configurations of C_1 and C_2 at mid plane of the tank (y=0).
(a) C_1=0.25D, C_2=0.4D, (b) C_1=0.3D, C_2=0.4D, (c) C_1=0.35D, C_2=0.45D, (d) C_1=0.4D, C_2=0.4D, (e) C_1=0.45D, C_2=0.4D

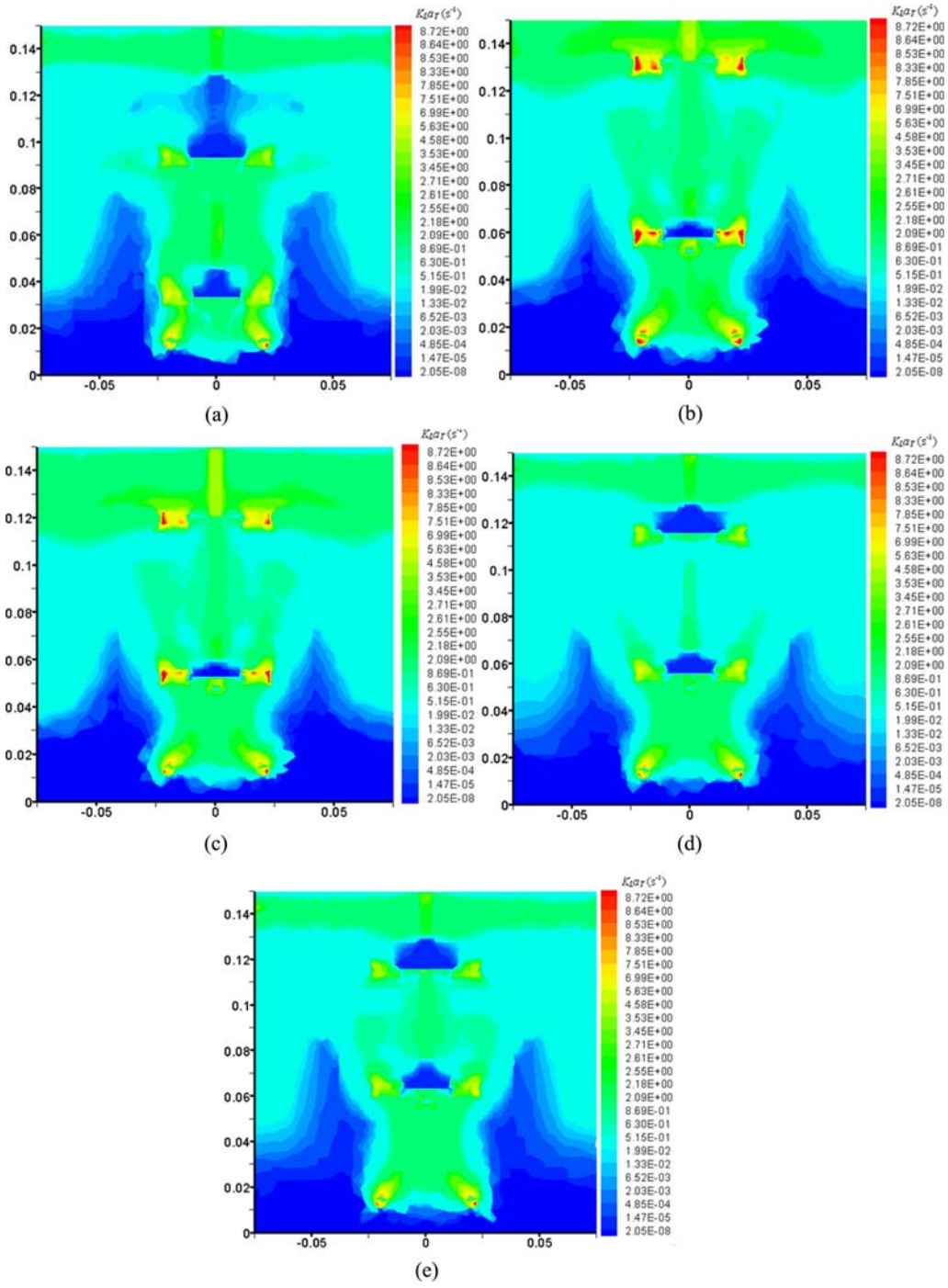

Fig. 7. Contours showing distribution of predicted K_La_{20}.
(a) C_1=0.25D, C_2=0.4D, (b) C_1=0.3D, C_2=0.4D, (c) C_1=0.35D, C_2=0.45D, (d) C_1=0.4D, C_2=0.4D, (e) C_1=0.45D, C_2=0.4D

movements are likely taking place in different directions when C_2 is fixed at 0.4D.

Fig. 7(a)-(e) shows the local distribution of K_La_{20} for different optimal C_1 and C_2 configurations.

Lesser amount of K_La_{20} is predicted at a small region just above the impeller blade except at two optimal points (C_1=0.3D & C_2= 0.4D and C_1=0.35D & C2=0.45D) and lower part of tank; K_La_T in such region ranges nearly from 0.01 to 0.00000002 s^{-1} which is a lesser amount as compared with other region of the vessel, i.e., average K_La_{20} ranges from 4.5 to 0.01 s^{-1}. Highest amount is predicted at the sparger and at impeller tip ranging from nearly 8.7 to 4.5 s^{-1} at all the cases of C_1 and C_2. The maximum amount of K_La_{20} is predicted comparably when C_1=0.3D & C_2=0.4D and C_1=0.35D and C2=0.45D among the other configuration as seen from Fig. 7(b) and (c). In these configurations, better mass transfer is seen predicted just above the upper impeller in contrast to other configuration where lowest K_La_{20} is predicted. This is an indication of better mixing of gas and liquid phase for better performance of the sys-

Table 2. Measured and predicted K_La_{20} at N=500 rpm

C_1	C_2	P_g/V	K_La_{20}			
			Expt.	van't Riet eqn.	CFD	Prediction error %
0.25D	0.4D	3322.01	0.0204	0.0211	0.0231	11.68
0.3D	0.4D	3586.26	0.0229	0.0217	0.0259	11.58
0.35D	0.45D	3397.51	0.0227	0.0213	0.0256	11.32
0.4D	0.4D	3284.26	0.0223	0.0210	0.0237	5.91
0.45D	0.35D	3699.51	0.0167	0.0220	0.0209	20.09

tem. The comparison of predicted K_La_{20} with observed value is in Table 2. There is fair agreement of predicted K_La_{20} with observed values and calculated value by using the van't Riet equation.

3. Development of Scale-up Criteria

Scale-up criteria have been developed for global optimal point, which is C_1=0.3D and C_2=0.4D. By maintaining geometrical similarity and global optimal impeller clearances, further experimentation was carried out to develop the scale up criteria. Geometrical similarity, which involves physical dimensions of the stirred tank, should be maintained constant while developing the scale up criteria. It can be achieved by doing experimentation on different sized stirred tanks, which eliminates the scale effect of dynamic variables. Scale up criteria for basic parameters (mass transfer rates, power ratio and gas holdup) are required to design a stirred tank, which can be obtained by deriving the functional form of these variables. The functional behavior of mass transfer and power consumption can be composed of the following influencing variables as:

$$\begin{pmatrix} K_La_{20} \\ \frac{P_g}{P_u} \end{pmatrix} = f(H, D, d, l, b, C_1, C_2, Q_g, N, g, v) \tag{20}$$

In non-dimensional form, Eq. (20) can be written as:

$$\begin{pmatrix} k_c \\ \frac{P_g}{P_u} \end{pmatrix} = f(H/D, d/D, l/d, b/d, C_1/D, C_2/D, Fl, Re, Fr) \tag{21}$$

With constant geometrical parameters, the functional form governing the process parameter can be reduced as:

$$\left.\begin{aligned} k_c &= f(Fl, Re, Fr) \\ \frac{P_g}{P_u} &= f(Re, Fr, Fl) \end{aligned}\right\} \tag{22}$$

where, Fl is Flow number ($Fl=Q_g/Nd^3$), Re is the impeller Reynolds number ($Re=Nd^2/\nu$) and Fr is the impeller Froude number ($Fr=N^2d/g$). Here, k_c is the non-dimensional mass transfer rate and is equal to $K_La_{20}(v/g^2)^{1/3}$. The intensity of turbulence and wave action on the water are the major factors normally associated with unbaffled stirred tanks. Turbulence and viscous effects are generally described by the Reynolds number (Re), whereas the surface wave action is described by the Froude number (Fr). Eq. (22) suggests that in order to eliminate the effect of scale, mass transfer rate and power consumption should be simulated by using all the three variables. In case of a gassed system (gas-liquid), the Froude number is significant as the gravitational forces tend to promote a vertical separation of liquid and gas phase [42]. Gravity acting on the liquid leaving an impeller traveling radially to the tank wall in gassed system will tend to promote the downward flow of the liquid producing an unsymmetrical flow pattern as opposed to that of single phase. Clark and Vermeulen [43] argued to include the Froude number in order to represent the surface behavior of flow in gas-liquid system. Deshmukh and Joshi [44] used both the Reynolds and Froude numbers in their correlation of the power number in a baffled circular surface aerator. Recently Scargiali et al. [45] also used Reynolds and Froude numbers in power number scaling of unbaffled stirred tanks. Reynolds and Froude number can be further combined into a new number $X(=Fr^{4/3}Re^{1/3})$, called theoretical power per unit volume [46]. Present work uses X to combine the Re and Fr in the scale up criteria. Thus Eq. (22) can be reduced as:

$$\left.\begin{aligned} k_c &= f(Fl, X) \\ \frac{P_g}{P_u} &= f(Fl, X) \end{aligned}\right\} \tag{23}$$

Gas holdup is also influenced by several variables of geometrical and operational parameters. In geometrical similar systems, the function governing gas holdup is as follows:

$$\varepsilon_G = f(Fl, P_v) \tag{24}$$

where, $P_v=P_g/(V\gamma(g\upsilon)^{1/3})$ is the non-dimensional form of effective power per unit volume, V is the volume of the tank.

The development of a global optimal point based on mass transfer rate was derived through experimentation on 150 mm tank. To develop scale up criteria, more experimentation was carried out on 150 mm and 200 mm. The purpose of doing experimentation on 200 mm tank is to eliminate the scale effect in dynamic variables. During development of scale up criteria, geometrical similarity was maintained the same in both the tanks. The measurement of process variables such as mass transfer rate, gassed to ungassed power and gas holdup were measured in both tanks. These experimental observations were subjected to least square regression to find the functional form of Eqs. (23) and (24). The functional form of the equations is as follows:

$$\left.\begin{aligned} 10^5 k_c &= 2.41 Fl^{0.03} X^{0.44} \\ \frac{P_g}{P_u} &= 0.57 Fl^{-0.005} X^{0.15} \\ \varepsilon_G &= 4.73 Fl^{0.009} P_v^{0.65} \end{aligned}\right\} \tag{25}$$

Statistical details of Eq. (9) are given in Table 3.

Table 3. Statistical details of Eq. (25)

Section	R^2	Standard error of the model	Residual sum of squares	Parameter estimate through regression	Standard error in estimation of parameter
k_c	0.98	1.92e-3	8.89e-5	2.41	0.008
				0.03	0.0031
				0.44	0.0023
P_g/P_u	0.98	1.39e-3	2.56e-5	0.57	0.074
				−0.005	0.0089
				0.15	0.0012
ε_G	0.94	2.56e-3	6.12e-5	4.73	0.028
				0.009	0.0052
				0.65	0.0015

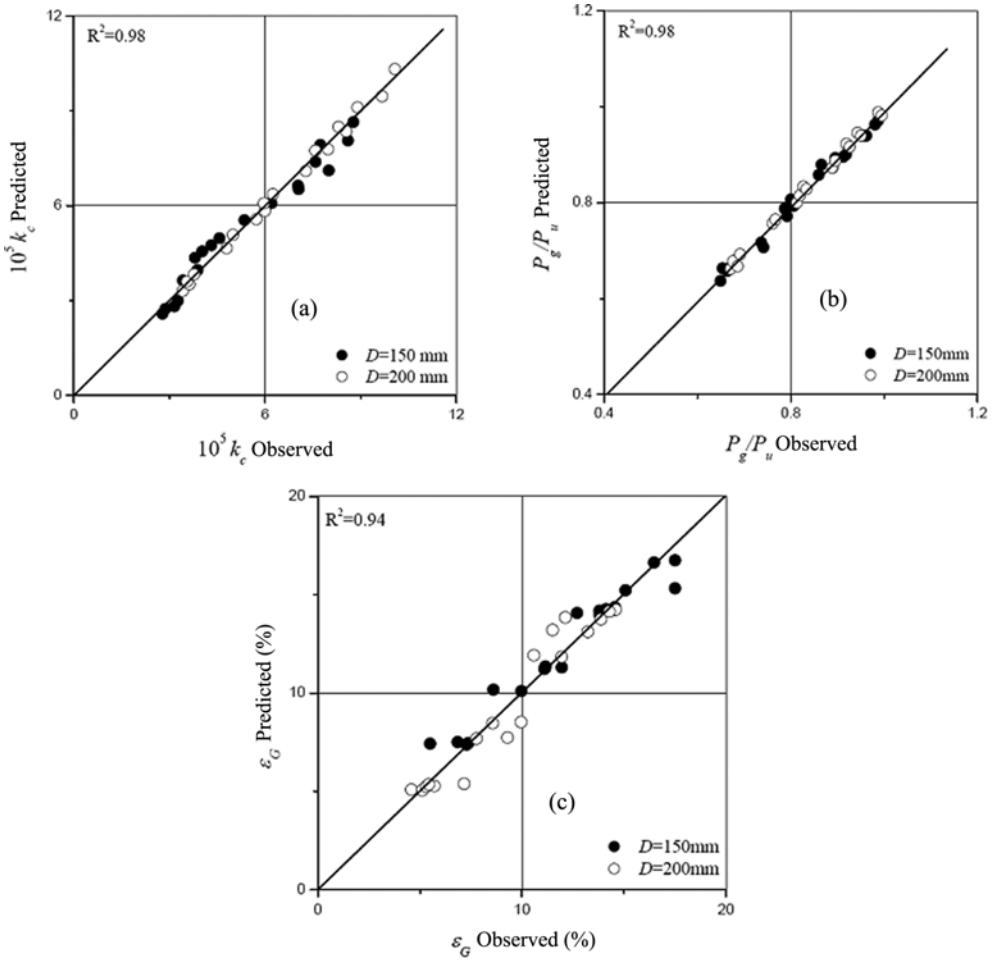

Fig. 8. Scale-up criteria (a) mass transfer and (b) power consumption and (c) gas holdup.

Standard error of parameters used in regression analysis indicates confidence for many engineering applications. The standard error of a parameter is the expected value of the standard deviation of that parameter if the experiment is repeated many times. It can be seen from the statistical details that the parameters are substantially uncertain, which makes them good leading indicators. Fig. 8 shows the parity plot of the process variables, which is a scatter plot of experimental observations against values derived through Eq. (25). The coefficient of determination between experimental values and predicted through Eq. (25) is quite high; thus it can be said that the derived functional forms uniquely simulate the process variables.

CONCLUSION

The double concave blade impeller system in sparged condition is experimentally studied. Optimal impeller spacings (C_1 and C_2) were found through univariant approach. Based on the optimal point, a scale-up criterion for each parameter was developed. After several

combinations of C_1 and C_2 were experimentally investigated based on K_La_{20}, the combination of optimal configurations of the system was found at C1=0.25D & C_2=0.4D, C_1=0.3D & C_2=0.4D, C_1= 0.35D & C_2=0.45D, C_1=0.4D, C_2=0.4D, C_1=0.45D & C_2=0.35D. Global optimum point because of highest K_La_{20} (0.0229 s^{-1}) is observed at C_1=0.3D & C_2=0.4D and minimum K_La_{20} (0.0167 s^{-1}) was observed at C_1=0.45D & C_2=0.35D. Based on the optimal configuration, flow patterns of the two phases and K_La_T were modeled through CFD tools. The behavior of the liquid flow in sparged system is totally different from single phase system. There is no formation of circulation loop predicted in this sparged condition except one loop above the lower impeller. Strong flow circulation of liquid and gas is predicted at the sparger, at the impeller tip and around the impeller region.

REFERENCES

1. P. R. Gogate, A. A. C. M. Beenackers and A. B. Pandit, *Biochem. Eng. J.*, **6**, 109 (2000).
2. D. Chen, L. Xu, G. Chen and S. Rong, *Chem. React. Eng. Technol.*, **8**, 44 (1992).
3. V. Hudcova, V. Machon and A. W. Nienow, *Biotechnol. Bioeng.*, **34**, 617 (1989).
4. K. Rutherford, C. Lee, S. M. Mahmoudi and M. Yianneskis, *AIChE J.*, **42**,332 (1996).
5. S. M. Mahmoudi, *Velocity and mixing characteristics of stirred vessels with two impellers*, Ph. D. Thesis, University of London, England (1994).
6. V. Linek, T. Moucha and J. Sinkule, *Chem. Eng. Sci.*, **51**, 3203 (1996).
7. Y. Q. Cui, R. G. J. M. VanderLans and K. C. A. M. Luyben, *Chem. Eng. Sci.*, **51**, 2631 (1996).
8. J. Markopoulos and E. Pantuflas, *Chem. Eng. Technol.*, **24**, 1147 (2001).
9. A. R. Khopkar and P. A. Tanguy, *Chem. Eng. Sci.*, **63**, 3810 (2008).
10. S. U. Ahmed, P. Ranganathan, A. Pandey and S. Sivaraman, *J. Biosci. Bioeng.*, **109**, 588 (2010).
11. M. Taghavi, R. Zadghaffari, J. Moghaddsa and Y. Moghaddas, *Chem. Eng. Res. Des.*, **89**, 280 (2011).
12. F. Saito, A. W. Nienow, S. Chatwin and I. P. T. Moore, *J. Chem. Eng.*, **25**, 281 (1992).
13. M. Cooke, J. C. Middleton and J. R. Bush, *Bioreactor fluid dynamics*, *Proceedings of 2nd Bioreactor Conference*, Cambridge, UK (BHRA), 37 (1988).
14. Z. D. Chen and J. J. J. Chen, *Chem. Eng. Res. Des.*, **77**, 104 (1999).
15. B. H. Junker, Z. Mann and G. Hunt, *Appl. Biochem. Biotechnol.*, **89**, 67 (2000).
16. B. Mazzarotta, *AIChE Symp. Ser.*, **89**,112 (1993).
17. J. M. Rousseaux, H. Muhr and E. Plasari, *Can. J. Chem. Eng.*, **79**, 697 (2001).
18. L. E. Aloi and R. S. Cherry, *Chem. Eng. Sci.*, **51**, 1523 (1996).
19. M. Assirelli, W. Bujalski, A. Eaglesham and A. W. Nienow, *Chem. Eng. Sci.*, **63**, 35 (2008).
20. F. Grisafi, A. Brucato and L. Rizzuti, *IChemE Symp. Ser.*, **136**, 571 (1994).
21. M. Yoshida, A. Kimura, K. Yamagiwa, A. Ohkawa and S. Tezura, *J. Fluid Sci. Technol.*, **3**, 282 (2008).
22. V. B. Rewatkar, A. J. Deshpande, A. B. Pandit and J. B. Joshi, *Can. J. Chem. Eng.*, **71**, 226 (1993).
23. M. S. Puthli, V. K. Rathod and A. B. Pandit, *Biochem. Eng. J.*, **23**, 25 (2005).
24. H. Djelal, F. Larher, G. Martin and A. Amrane, *J. Biotechnol.*, **125**, 95 (2006).
25. F. Garcia-Ochoa and E. Gomez, *Biotechnol. Adv.*, **27**, 153 (2009).
26. S. S. Patil, N. A. Deshmukh and J. B. Joshi, *Ind. Eng. Chem. Res.*, **43**, 2765 (2004).
27. G. Ascanio, B. Castro and E. Galindo, *Chem. Eng. Res. Des.*, **82**, 1282 (2004).
28. R. L. King, R. A. Hiller and G. B. Tatterson, *AIChE J.*, **34**, 506 (1988).
29. D. A. Deglon and C. J. Meyer, *Miner. Eng.*, **19**, 1059 (2006).
30. D. A. Drew, *Annu. Rev. Fluid Mech.*, **15**, 261 (1983).
31. A. R. Khopkar, G. R. Kasat, A. B. Pandit and V. V. Ranade, *Chem. Eng. Sci.*, **61**, 2921 (2006).
32. J. C. Scargiali, F. D'Orazio, F. Grisafi and A. Brucato, *Chem. Eng. Res. Des.*, **85**, 637 (2007).
33. G. Montante, A. Paglianti and F. Magelli, *Chem. Eng. Res. Des.*, **85**, 647 (2007).
34. V. V. Ranade, *Computational flow modeling for chemical reactor engineering*, Process Systems Engineering Series, Academic Press, New York (2002).
35. F. Kerdouss, A. Bannari and P. Proulx, *Chem. Eng. Sci.*, **61**, 3313 (2006).
36. S. E. Elgobashi and M. A. Rizk, *Int. J. Multiph. Flow*, **15**, 119 (1989).
37. Fluent 6.3 User's Guide, 2006.
38. C. Simonin and P. L.Viollet, *Numerical Methods for Multiphase Flows*, **91**, 65 (1990).
39. M. Bakker and H. E.Van Den Akker, *Transactions of IChemE*, **72**, 594 (1994).
40. F. Kerdouss, A. Bannari, P. Proulx, R. Bannari, M. Skrga and Y. Labrecque, *Comput. Chem. Eng.*, **32**, 1943 (2008).
41. M. Ishii and N. Zuber, *AIChE J.*, **25**, 843 (1979).
42. D. J. Gray, R. E. Treybal and S. M. Barnett, *AIChE J.*, **28**, 195 (1982).
43. M. W. Clark and T. Vermeulen, *AIChE J.*, **10**, 420 (1964).
44. N. A. Deshmukh and J. B. Joshi, *Chem. Eng. Res. Des.*, **84**, 977 (2006).
45. F. Scargiali, A. Busciglio, F. Grisafi, A. Tamburini, G. Micale and A. Brucato, *Ind. Eng. Chem. Res.*, **52**, 14998 (2013).
46. A. R. K. Rao and B. Kumar, *Korean J. Chem. Eng.*, **25**, 1338 (2008).